

Cite this: *J. Mater. Chem. A*, 2015, 3, 7437

# Magnetic molecularly imprinted microsensor for selective recognition and transport of fluorescent phycocyanin in seawater†

Zhong Zhang,<sup>ab</sup> Jinhua Li,<sup>a</sup> Longwen Fu,<sup>a</sup> Dongyan Liu<sup>a</sup> and Lingxin Chen<sup>\*a</sup>

Phycocyanin with excellent fluorescence characteristics and important physiological significance is an effective indicator for cyanobacterial bloom assessment due to its close relationship with cyanobacterial biomass. Molecularly imprinted polymers (MIPs) have attracted great interest owing to their recognition specificity; micromotor-driven targeted transport capability holds considerable promise. Herein, we propose an attractive magnetic microsensor for selective recognition, enrichment and transport of label-free fluorescent phycocyanin by combining MIPs and catalytic micromotors. The MIP-based catalytic microsensor was fabricated using phycocyanin as the imprinting molecule, Ni (0.55%) as the magnetic navigation material, and Pt (24.55%) as the solid support/catalyst to facilitate free movement in solutions, as well as an additional magnetic field was employed for trajectory control. The autonomous self-propulsion microsensor vividly displayed their motion states, presenting two different trajectories. The movement velocity was calculated based on the body-deformation model, suggesting a linear positive correlation between the velocity and hydrogen peroxide concentration, with a high average speed of  $163 \mu\text{m s}^{-1}$ . In addition, highly efficient targeted identification and enrichment abilities were demonstrated based on the magnetically imprinted layer. More excitingly, no obvious interference was found from complicated matrices such as seawater samples, along with real-time visualization of phycocyanin loading and transport. The sensing strategy would not only provide potential applications for rapid microscale monitoring of algae blooms, but also enrich the research connotations of protein imprinting.

Received 7th January 2015  
Accepted 25th February 2015

DOI: 10.1039/c5ta00143a

[www.rsc.org/MaterialsA](http://www.rsc.org/MaterialsA)

## 1. Introduction

Cyanobacterial blooms are one of the major adverse events for inland waters because of the eutrophication processes induced by urbanization, industrial and agricultural activities.<sup>1</sup> Phycocyanin, a blue colored photosynthetic accessory pigment protein, displays important biological significance,<sup>2</sup> and is also an effective indicator for the cyanobacterial bloom assessment due to its close relationship with cyanobacterial biomass.<sup>3</sup> Hence, recognition, determination and removal of phycocyanin are being increasingly investigated since the monitoring and remediation of cyanobacterial blooms has become a crucial global issue.<sup>4,5</sup> Phycocyanin emits fluorescence at about 615–640 nm, has a high absorption coefficient in a wider spectral range, and is stable in water for a long time. So, this protein has

become a new desirable fluorescent marker with high stability and sensitivity and can be applied in many aspects especially life, biomedical and environmental sciences.<sup>6,7</sup> Therefore, we also aspire to perform related fluorescence sensing studies on phycocyanin.

Molecular imprinting technology has attracted great interest owing to its unique properties of structure predictability, recognition specificity and application universality, and these features have been displayed by molecularly imprinted polymers (MIPs).<sup>8–10</sup> Recently, MIPs on the surface of matrices have displayed excellent properties especially for protein imprinting.<sup>9,11</sup> Compared to traditional MIPs, surface imprinted polymers have some special advantages such as more complete template removal, better site accessibility and lower mass transfer resistance, and thereby higher selective enrichment ability.<sup>12–14</sup>

In recent years, catalytic micro/nanomotors have witnessed bigger developments in motion control, in which magnetic materials can generally be used to control the movement and achieve a predetermined path.<sup>15,16</sup> So, excitedly, the coupling of surface imprinting and micro/nanomotor preparation technologies can provide tailor-made self-propelled micro/nanomotors with predetermined specificities for selective capture and

<sup>a</sup>Key Laboratory of Coastal Environmental Processes and Ecological Remediation, Shandong Provincial Key Laboratory of Coastal Environmental Processes, Yantai Institute of Coastal Zone Research, Chinese Academy of Sciences, Yantai 264003, China. E-mail: lxchen@yic.ac.cn; Fax: +86 535 2109130; Tel: +86 535 2109130

<sup>b</sup>University of Chinese Academy of Sciences, Beijing 100049, China

† Electronic supplementary information (ESI) available. See DOI: 10.1039/c5ta00143a

transport of targets. Compared to traditional biological molecular motors, the imprinted catalytic micro/nanomotors prepared by the present synthesis and preparation processes are simpler, controllable, have longer working life, good reproducibility and low environmental requirements, and facilitate functionalization and integration.<sup>17</sup> Besides, the recognition properties of the synthetic imprinted micro/nanomotors can withstand harsher conditions than their natural counterparts, which make the MIP-based micro/nanomotors especially attractive for diverse practical applications. In addition, hydrogen peroxide fuel can affect the stability and recognition properties of biological molecular motors, but it has almost no effect on the MIP ones.<sup>18</sup> However, to the best of our knowledge, few studies combining micromotors and molecular imprinting have been reported.<sup>19</sup> Accordingly, we expect to construct a new simple MIP-based label-free fluorescent micromotor sensor that can recognize and transport some special proteins, such as phycocyanin.

Herein, we develop a simple, magnetic surface-imprinted micromotor fluorescent sensor by the integration of molecular imprinting and catalytic micromotors for convenient, rapid and sensitive recognition and transport of phycocyanin in seawater. Phycocyanin is selected as the imprinting molecule and the label-free fluorescent marker, and hydrogen peroxide for catalytic propulsion. The present microsensor mainly profits from the following advantages: (i) simple preparation, without involving chemical reactions or harsh conditions, (ii) excellent control of the polymerization and localization of the microstructures by electrosynthesis, (iii) the specific electroensing polymeric material exhibits 3D microstructures and superior resistance against nonspecific protein adsorption, and finally provides good binding capacity and sensitivity, and (iv) it is reasonable to expect that the system is scalable down to the nanosize. The microsensor is fully characterized by SEM, EDS of samples, fluorescence spectroscopy/microscopy and confocal laser scanning microscopy. The motion control capacity and fluorescence detectability are investigated in detail. Moreover, the magnetically imprinted microsensor is successfully applied to complex seawater sample analysis and provides satisfactory real-time visualization of phycocyanin loading and transport.

## 2. Experimental

### 2.1 Reagents and materials

Phycocyanin was kindly provided by Shandong Oriental Ocean Company (Yantai, China) and used as the template protein. Bovine serum albumin (BSA), 3,4-ethylenedioxythiophene (EDOT), poly(sodium-4-styrenesulfonate) (NaPSS, MW ~ 70 000), sodium cholate, nickel aminosulfonate ( $\text{Ni}(\text{H}_2\text{NSO}_3)_2 \cdot 4\text{H}_2\text{O}$ ), and sodium dodecyl sulfate (SDS, MW 288.38 g mol<sup>-1</sup>) were purchased from Sigma-Aldrich (Shanghai, China). Hydrogen peroxide ( $\text{H}_2\text{O}_2$ ), chloroplatinic acid ( $\text{H}_2\text{PtCl}_6$ ), lead nitrate ( $\text{Pb}(\text{NO}_3)_2$ ), hydrochloric acid (HCl), ethanol, Tween-20, boron hydrogen acid ( $\text{H}_3\text{BO}_3$ ), dichloromethane, nickel chloride, potassium chloride and other affiliated chemicals were all obtained from Sinopharm Chemical Reagent Co. Ltd. (Shanghai, China). All solvents and chemicals were of analytical

grade and used directly without further purification unless otherwise specified. Doubly purified deionized water (18.2 M $\Omega$ , Millipore, MA, USA) was used for the preparation of all aqueous solutions.

A cyclopore polycarbonate membrane, containing conical-shaped ordered micropores of 2  $\mu\text{m}$  diameter (Catalog no. 7060-2511; Whatman, Maidstone, U.K.), was employed as the template. Platinum plating solution consisted of 33 mmol L<sup>-1</sup>  $\text{H}_2\text{PtCl}_6$ , 33  $\mu\text{mol L}^{-1}$   $\text{Pb}(\text{NO}_3)_2$ , and 0.5 mol L<sup>-1</sup> HCl. Nickel plating solution consisted of 84 mmol L<sup>-1</sup>  $\text{NiCl}_2 \cdot 6\text{H}_2\text{O}$ , 1.6 mol L<sup>-1</sup>  $\text{Ni}(\text{H}_2\text{NSO}_3)_2 \cdot 4\text{H}_2\text{O}$ , and 322 mmol L<sup>-1</sup>  $\text{H}_3\text{BO}_3$ . The Pt-Ni mixture solution was prepared by mixing equal volumes of the platinum plating solution and nickel plating solution. The washing solution (PBST-20X) consisted of 0.05 mmol L<sup>-1</sup> phosphate buffer solution (PBS, pH 7.0), containing 0.15 mol L<sup>-1</sup> potassium chloride and 0.05% Tween-20.

### 2.2 Fabrication of the electrochemical cell device

An electrochemical cell was utilized for the deposition of electronic conductive polymer and metal materials into the micropores of the membrane. The electrochemical cell was custom-built and designed using Teflon to resist chemical corrosion, similar to a reported procedure<sup>20</sup> with some modifications. Fig. S1A and B† show the top view and lateral view photographs, respectively. As seen, the prepared cell could hold about 8 mL solutions. The principal aim of the cell is to hold the Pt-coated side of the membrane in place as the working electrode in the electroplating solution along with the reference and counter electrodes. The dimensions were chosen to make full use of the polycarbonate membrane while maximizing the surface area for plating. By electrochemically reducing metal ions,  $\text{Ni}^{2+}$  and  $\text{Pt}^{4+}$ , from the solution into the Pt-packed pores of the membrane template, microtubules could grow with thickness increasing with the increase of applied charges.

For the most part, the designed cell worked well in this system. The synthesis of magnetically imprinted micromotors proved to be reproducible, and a simple adjustment of either the current upper limit or polymerization time provided consistent results. A commercial polycarbonate membrane was used as the template, with a filtration pore structure of 2  $\mu\text{m}$  diameter on both sides and 20  $\mu\text{m}$  thickness. Such a polycarbonate membrane could provide an attractive template structure, as required for the bubbling propulsion mechanism.<sup>21</sup> SEM images of the front and back of the polycarbonate membrane are shown in Fig. S1C and D.† The polycarbonate membrane was sputtered with the Pt layer on one of its back sides to provide conductivity and thereby to be used as a working electrode. The polycarbonate membrane after being sputtered with a conductive Pt layer is shown in Fig. S1E and F.† So, all these photograph and image results proved that the membrane can be used as an ideal template in the template electrochemical deposition method.

### 2.3 Processing of the polycarbonate membrane

The polycarbonate membrane was sputtered with a Pt layer on the dark side to provide conductivity and was used as the

working electrode, and then it was put in 20 mL phycocyanin protein solution ( $0.5 \text{ mg mL}^{-1}$ ). After ultrasonic processing for 3 min to remove the air in the micropores, the membrane was incubated at  $25^\circ\text{C}$  for 30 min. Electrostatic forces would drive the phycocyanin to filter into the space in the ordered micropores, and the pore surface of the polycarbonate membrane was fully filled with the protein solution. The membrane was dried in air for 20 min. After being sequentially rinsed with water, PBST-20X and water, the membrane was then assembled in a custom-built plating cell with an aluminum foil serving as a contact with the Pt layer. A Pt wire and an Ag/AgCl electrode ( $3 \text{ mol L}^{-1} \text{ KCl}$ ) served as the counter and reference electrodes, respectively.

#### 2.4 Preparation of tubular micromotors

Tubular micromotors were prepared by the template electrochemical deposition method following the process of the five step electrodeposition protocol similar to a reported procedure<sup>19,22</sup> with necessary modification. Briefly, poly(3,4-ethylenedioxythiophene) (PEDOT) layers were first deposited potentiostatically for 574 s at  $+0.80 \text{ V}$  using a charge of 4 C from a plating solution containing 10 mM EDOT and 125 mM NaPSS. Subsequently, an initial Pt layer was deposited galvanostatically at  $-2 \text{ mA}$  for 200 s from a platinum plating solution to improve the mechanical properties of the polymeric layer. Then, an additional Pt–Ni layer was deposited galvanostatically at  $-2 \text{ mA}$  for 300 s from a Pt–Ni mixture solution to provide a smooth and highly conductive surface after the polymer deposition and improve the deposition of subsequent metallic layers. An intermediate Ni layer was then deposited potentiostatically at  $-1.3 \text{ V}$  for 2.0 C from a Ni plating solution to provide magnetic guidance. Finally, the inner catalytic Pt layer was deposited galvanostatically at  $-2 \text{ mA}$  for 450 s. The related parameters are listed in Table S1.†

#### 2.5 Preparation of the magnetically imprinted microsensor

The deposited membrane was taken out from the electrochemical cell, and the sputtered Pt layer on the dark side of the membrane was completely removed by hand polishing with 3–4  $\mu\text{m}$  alumina powder. The resulting PEDOT–Pt–Ni–Pt multilayer microtubes were released from the membrane by immersion in a dichloromethane solvent that also removes the template protein, leaving imprinted nanocavities on their outermost surface. After completely dissolving the membrane and removing the protein template, the magnetically imprinted micromotors were separated from membrane micropores. The micromotors were rinsed twice with dichloromethane, ethanol and ultrapure water, respectively, and were collected by centrifugation at 6000 rpm for 3 min. All magnetically imprinted micromotors were stored in ultrapure water at room temperature until use. As a control, magnetically non-imprinted polymer (NIP) micromotors were also prepared under identical conditions without phycocyanin molecules in the reaction system.

#### 2.6 Characterization of the magnetically imprinted microsensor

Ion sputter (E-1045, HITACHI) was used to sputter the polycarbonate membrane with a platinum layer. The procedure was performed at room temperature under a base vacuum of 7.0 Pa, an electric current of 15 mA and a sputtering time of 200 s. The microscopic morphologies of the magnetically imprinted micromotors were observed by scanning electron microscopy (SEM, JSM 5600 LV, 5 kV). All samples were sputter-coated with gold before SEM analysis. Elemental analysis was carried out with an energy dispersive X-ray microanalyzer (EDS) on a scanning electron microscope to confirm the multilayer content. A fluorescence microscope (BX61, Olympus) was employed to observe the fluorescence microscopy image of the sample on a glass slide equipped with a CCD camera, a  $20\times$  objective (unless mentioned otherwise) and acquired at a frame rate of 10 frames per second using the SPOT Advanced 4.6 software, which was used to capture fluorescence images. Further observations and videos were recorded and captured by using a confocal laser scanning microscope (CLSM) (FV1000, Olympus). The protein coverage on the micromotors was estimated by fluorescence qualitative analysis using the corresponding time-lapse images obtained using the ImageJ software (where 100% means complete fluorescent coverage of the exposed surface). The average fluorescence-intensity values were obtained from triplicate independent results used for the following discussion.

#### 2.7 Batch procedure of fluorescent protein recognition properties

To evaluate the protein recognition properties of the magnetically imprinted micromotors, adsorption time, phycocyanin concentration, sodium cholate and hydrogen peroxide concentrations were investigated by a batch method. The procedures for phycocyanin concentration determination were carried out as follows. 50  $\mu\text{L}$  of magnetically imprinted micromotor solution was centrifuged at 6000 rpm for 3 min to remove the supernatant, and equilibrated with 50  $\mu\text{L}$  phycocyanin solutions with concentrations varying from 0.5 to  $1 \text{ mg mL}^{-1}$  in  $0.05 \text{ mol L}^{-1}$  phosphate buffer solution (pH 7.0) for 30 min. The supernatants were removed by centrifugation, and then the micromotors were collected and re-suspended in 50  $\mu\text{L}$  of phosphate buffer ( $0.05 \text{ mol L}^{-1}$ , pH 7.0). 5  $\mu\text{L}$  of the solution mixture was placed on a glass slide and observed with a fluorescence microscope.

In order to determine the dependence of surface coverage on the adsorption time, related experiments were conducted as described below. 2  $\mu\text{L}$  of the magnetically imprinted micromotor solution equilibrated with 2  $\mu\text{L}$  of  $0.5 \text{ mg mL}^{-1}$  phycocyanin was placed on a glass slide. The solution was observed with the fluorescence microscope with a  $20\times$  objective for 0, 5, 10, 15, 20, and 25 min, respectively, and then the fluorescence on the surface of the micromotor was captured by time-lapse photos. The corresponding photos were utilized to determine phycocyanin surface coverage on the micromotors with adsorption time change using ImageJ software.

The capture and transport experiments were performed by using CLSM. The magnetically imprinted micromotor solution consisted of four solutions, including 2  $\mu\text{L}$  of magnetically imprinted micromotors, 2  $\mu\text{L}$  of 3% sodium cholate, 2  $\mu\text{L}$  of 3%  $\text{H}_2\text{O}_2$  and 2  $\mu\text{L}$  of phycocyanin (1  $\text{mg mL}^{-1}$ ) solution, which were successively added dropwise onto a glass slide. The fluorescence images of moving micromotors were collected and captured in a video.

### 3. Results and discussion

#### 3.1 Preparation and characterization of the magnetically imprinted microsensors

The magnetically imprinted micromotor sensor was prepared by using a modified template electrochemical deposition method,<sup>19,22</sup> as illustrated in Fig. 1. The procedure involves the processing of the polycarbonate membrane (Fig. 1A and B), five-step electrochemical deposition (Fig. 1C), and the construction of the magnetically imprinted micromotor (Fig. 1D and E). The critical step for selective recognition and controllable self-propelled ability of microtubules is the five-step electrochemical deposition of various materials. The surface-imprinted PEDOT doped with the PSS complex is ideal for imprinting protein targets, because the matrix shows low nonspecific protein adsorption, and offers clear advantages in terms of controlling the deposition process and compatibility with aqueous media. The outer tubular PEDOT layer of micromotors was grown on the inner walls of the polycarbonate membrane micropores, which contained the pre-adsorbed phycocyanin molecules. The outer layer was formed by sequential electrodeposition of the inner Pt, Pt–Ni, Ni and Pt metallic layers.

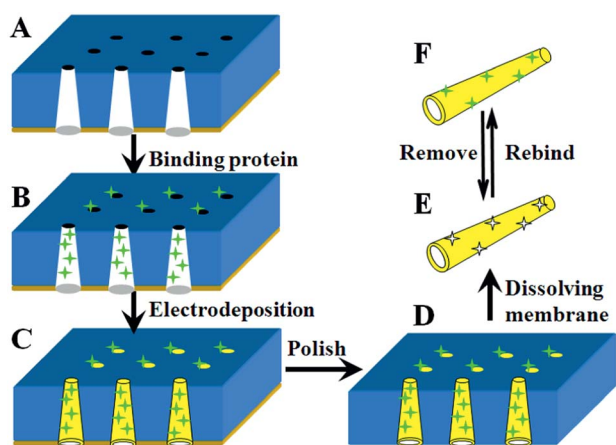


Fig. 1 Schematic illustration of the preparation process of the magnetically imprinted microsensors. (A) Sputtering a conductive Pt layer on the polycarbonate membrane, (B) the polycarbonate membrane adsorbs the negatively charged protein by electrostatic interactions, (C) sequential deposition is used to deposit the PEDOT/PSS, inner Pt, Pt–Ni, Ni and Pt layers, (D) the conductive Pt layer is completely removed by hand polishing, (E) the resulting PEDOT–Pt–Ni–Pt multilayer microtubules are released from the membrane by immersion in dichloromethane as well as the template proteins are removed, and (F) magnetically imprinted micromotors adsorb the template protein.

Among them, Ni was used for magnetic guidance; Pt was used as the micromotor skeleton and as a catalyst to produce the oxygen-bubble to supply propulsion power. Then the sputtered conductive Pt layer on the dark side of the membrane was completely removed by hand polishing. Finally, the magnetically imprinted micromotor sensor was obtained by dissolving the membrane and removing the protein template molecules (Fig. 1E). The microsensor with specific cavities could specifically and easily interact with the phycocyanin molecule through hydrogen bonds and electrostatic interactions (Fig. 1F).

SEM images of the typical conical micromotor sensor are displayed in Fig. 2. As seen in the side-view (A and B) and the cross-view (C), the MIP-based microsensor had a defined geometry with two-end outer diameters of 1.8 and 1.0  $\mu\text{m}$ , along with inner openings of 1.5 and 0.7  $\mu\text{m}$ , and a total length of 18  $\mu\text{m}$ . The MIP microsensor exhibited a highly rough outside polymeric surface (Fig. 2C), reflecting a large number of exposed complementary imprinted cavities on the surface of the micromotor. In contrast, a much smoother surface was observed on the NIP micromotor (Fig. 2D). The difference proved that the MIP-based micromotor had a much larger specific area than that of the corresponding NIP one, suggesting

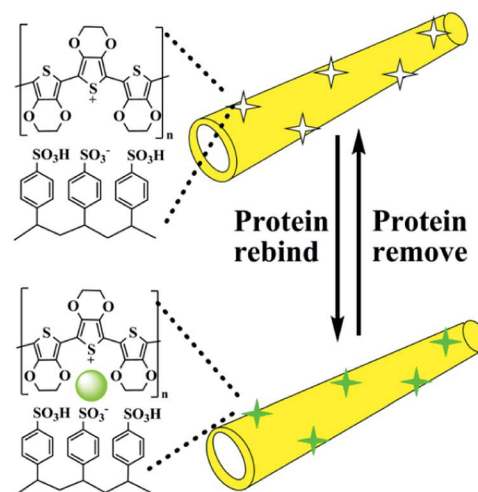
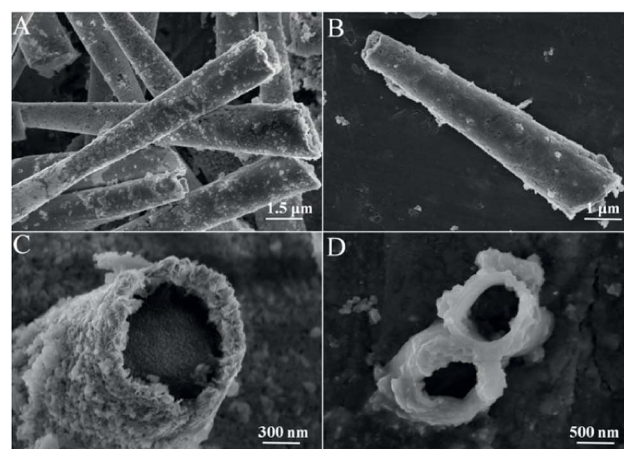


Fig. 2 (Upper) SEM images of the magnetic (A–C) MIP micromotor and (D) the NIP micromotor. (Lower) Scheme of the magnetic MIP micromotor used to rebind and remove protein.



that more additional binding sites were produced by eluting the template molecules of MIPs. Meanwhile, the essential conical shape of the micromotor was retained following the imprinting process.

EDS analysis was carried out to confirm the electrodeposition of materials, as recorded in Table S2.† All the plating solutions could be electroplated into the shell of the micromotor, the thickness of which was increased by increasing the charge. Continuous transformation of plating solutions of different metal ions with one another allowed one to deliberately and systematically prepare multilayer microtubules. The presence of both oxygen (27.0%) and carbon (46.7%) was from organic materials. PEDOT/PSS, Ni (0.55%) and Pt (24.55%) were electrochemically reduced from the plating solution into the conical microtubules, and Pb (0.40%) as a modifier of platinum plating solution was found as well. The experimental data in Table S2† were able to provide direct evidence for the successful growth of the multilayer micromotor. Therefore, a magnetically imprinted micromotor sensor was successfully obtained based on the template electrochemical deposition method.

### 3.2 Optimization of motion control conditions of the microsensor

The major factors influencing the motion conditions of micromotors generally include the surfactant,  $\text{H}_2\text{O}_2$  concentration, magnetic field, and micromotor shape.<sup>23,24</sup> In this work, the micromotor shape was determined by the membrane template, which had been fixed; according to preliminary experimental results, 1%  $\text{H}_2\text{O}_2$  was used. So, herein, the surfactant and magnetic field were carefully taken into account to achieve the optimal conditions for desired motion trajectories.

The surfactant effect was examined for the motion of the micromotor in 1%  $\text{H}_2\text{O}_2$ . Due to the high surface tension of water, the produced  $\text{O}_2$  bubbles were usually big in water, which neither was in favour of the observation of the microtubule movement status, nor facilitated the diffusion of fresh  $\text{H}_2\text{O}_2$  solution into the interior of the microtubules. So, herein, the sodium cholate surfactant was used to control the diameters of the oxygen bubbles produced in  $\text{H}_2\text{O}_2$  solution, and to promote the exchange of  $\text{H}_2\text{O}_2$  solution both inside and outside the microtubules, thereby replenishing fresh  $\text{H}_2\text{O}_2$  solution into microtubules to speed up the movement of microtubules. The surfactant effect on the oxygen bubbles was investigated. As seen in Fig. S2A–C,† the oxygen bubble diameter reduced from more than 150 to 20  $\mu\text{m}$  with increasing surfactant concentrations. When the concentration of sodium cholate exceeded a fixed value, the size of the bubbles did not reduce any more (Fig. S2D†), and then it was decided by the structure of the microtubules. Finally, the most favourable surface morphology and motion trajectories were obtained by using 1%  $\text{H}_2\text{O}_2$  in the presence of sodium cholate at 2%.

As seen, Fig. 3 and ESI Video 1† illustrate the obtained motion trajectories of the high propulsion power magnetically imprinted micromotor. The micromotor showed two types of motion trajectories: one was a straight trajectory with long oxygen bubble tails, which were released from the wider tubular

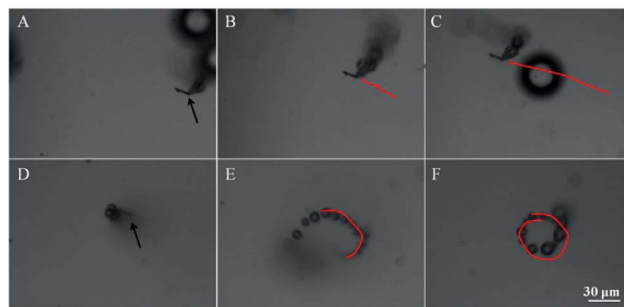


Fig. 3 Motion images of the micromotor propelling in the solution with (A–C) straight and (D–F) spiral motion trajectories. Red traces denote the path travelled by the micromotor.

openings, as shown in Fig. 3A–C; the other was a spiral and circular trajectory, with a high average speed of  $113 \mu\text{m s}^{-1}$ , as shown in Fig. 3D–F. The micromotor exhibited various motion trajectories depending on the distribution of platinum inside the tubes, as shown in ESI Video 1.† The mechanism responsible for these motions can be explained by the assumptions that the spatial unbalance of force or torque affects motion trajectories.<sup>25</sup> The propulsion force was controlled by the catalytic activity of platinum, and constant force/torque would be produced in the same manner as in composite motors. For example, when the platinum in the interior of the microtubule was not uniform, and thereby uneven bubble production in different places, the micromotor would exhibit circular, spin, and rotation motions. If platinum showed uniform distribution in the interior of the microtubules, it would move in straight trajectories.

Then, in the above optimized solutions, the magnetic field effect was investigated. ESI Video 2† shows time-lapse images of the micromotor motion under a magnetic field in the presence of 1%  $\text{H}_2\text{O}_2$  and 2% sodium cholate. As seen from the video, while the imprinted micromotor moved randomly, it was also possible to guide them magnetically by the intermediate ferromagnetic Ni layer. The micromotor moved rapidly in a straight trajectory at first, and then it moved in a curved trajectory after a magnet was placed on one side of the micromotor (ESI Video 2†). So, the imprinted micromotor sensor was demonstrated to be capable of directional motion effectively guided by magnetic fields.

### 3.3 Motion mechanism of the microsensor

To figure out what the motion velocity of the micromotor sensor depended on, it was required to quantitatively determine the bubble generation frequency and the average moving step length caused by the bubble ejection. The mechanism may be inferred from the fact that the bubble expelling frequency depended upon the production rate of oxygen ( $\text{O}_2$ ) and the bubble size, which was applicable to the present two types of motion trajectories. The production rate could be determined experimentally by measuring the volume of the produced  $\text{O}_2$  from a planar Pt surface with a predefined area.

The experimental results indicated that the productivity of  $\text{O}_2$  could be linearly proportional to the area of the Pt surface

and the  $\text{H}_2\text{O}_2$  concentration,  $C_{\text{H}_2\text{O}_2}$ . The average velocity of the micromotor moving in the  $\text{H}_2\text{O}_2$  solution,  $v_m$ , could be expressed referring to that reported as follows:<sup>21</sup>

$$v_m = f \times l = \frac{9nC_{\text{H}_2\text{O}_2}R_mL}{3R_b^2 + LR_b \left/ \left( \ln\left(\frac{2L}{R_m}\right) - 0.72 \right) \right.} \quad (1)$$

where  $f$  is defined as the bubble generation frequency,  $l$  is the average moving step length,  $n$  is the  $\text{O}_2$  rate constant,  $C_{\text{H}_2\text{O}_2}$  means the  $\text{H}_2\text{O}_2$  concentration,  $L$  is the micromotor length,  $R_m$  is the radius of the tubular cavity, and  $R_b$  indicates the average radius of the bubble.

According to eqn (1), we could predict that the average micromotor velocity  $v_m$  was linearly proportional to  $C_{\text{H}_2\text{O}_2}$  and also depended upon the micromotor length  $L$  and the micromotor radius  $R_m$ . Also, the catalytic motion of micromotors in the  $\text{H}_2\text{O}_2$  solution was indicated to be complex, and the velocity was influenced by a number of experimental parameters, especially the micromotor geometry and the chemical environment.

Furthermore, under the present conditions,  $n$  could be experimentally estimated to be  $9.8 \times 10^{-4} \text{ m s}^{-1}$  from both flat and rolled surfaces in  $\text{H}_2\text{O}_2$  with concentrations up to 10%. And the micromotor length  $L$  could be  $18 \mu\text{m}$ , the radius of the tubular cavity  $R_m$  could be  $1.5 \mu\text{m}$ , and the equivalent bubble radius  $R_b$  should be larger than the radius of the microjet  $R_j$ . And when the  $\text{H}_2\text{O}_2$  concentration  $C_{\text{H}_2\text{O}_2}$  was below than 3% in the experiments, the results could fit well with the relationship,  $R_b = 1.2R_m$ . Hence, eqn (1) could also be simplified as follows:

$$v_m = 1.04 \times 10^{-2} C_{\text{H}_2\text{O}_2} \quad (2)$$

As seen from eqn (2), the  $\text{H}_2\text{O}_2$  concentration could strongly influence the velocity of the catalytic micromotors. Our further experimental results showed that the average moving speed of the micromotor increased from  $113 \mu\text{m s}^{-1}$  at 1%  $\text{H}_2\text{O}_2$  to  $163 \mu\text{m s}^{-1}$  at 1.5%  $\text{H}_2\text{O}_2$ , as illustrated in ESI Video 3.† Correspondingly, it could be calculated according to eqn (2) that the moving speed increased from 104 to  $156 \mu\text{m s}^{-1}$ , respectively. Good fitting between experimental and calculated results proved the validity of the equations. Therefore, it could be concluded that the body-deformation model<sup>26</sup> was considered to be satisfactory and feasible.

### 3.4 Binding properties of the magnetically imprinted microsensor

Based on the above studies, such motion based isolation routes could enable direct visualization of the binding events based on the movement of the micromotor sensor. The existence of phycocyanin binding sites on the outside surface of the microsensor was confirmed by adsorption isotherm experiments, and the binding properties were investigated as follows.

The micromotor was incubated in  $0.5 \text{ mg mL}^{-1}$  phycocyanin solution over time. The imprinted polymeric layer was capable of selectively capturing the fluorescent target protein onto the micromotor, and then the micromotor could emit red fluorescence under UV light observed using a fluorescence microscope.

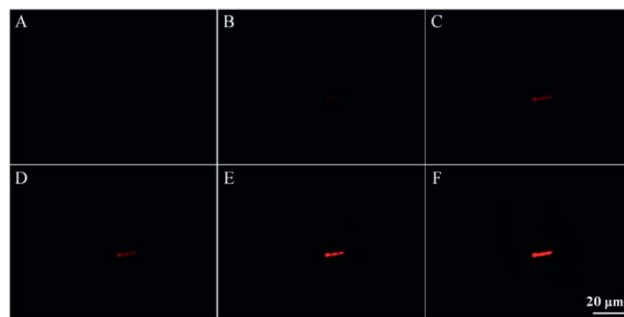


Fig. 4 Fluorescence microscope photos of the magnetically imprinted micromotor in the phycocyanin protein solution during the different time periods of (A) 0, (B) 5, (C) 10, (D) 15, (E) 20, and (F) 25 min. Experimental conditions: time-lapse images each taken over a 5 s period; phycocyanin protein solution concentration was  $0.5 \text{ mg mL}^{-1}$ .

Such capture is illustrated in Fig. 4A–F, which shows the influence of time on the adsorption capacity, estimated from the fluorescence coverage. The time-lapse images illustrated that the surface coverage had relatively low initial adsorption rates and then linearly increasing rates with time up to 20 min (Fig. 4A–E). It was observed that complete fluorescence coverage was achieved within 25 min (Fig. 4F), and the adsorption kinetics proved favourable and rapid.

This phenomenon could be explained as follows: by combining surface imprinting with PEDOT/PSS, most recognition sites were situated on the outside surface of the micromotor, which facilitated mass transfer and capturing. Therefore, the formation of surface-imprinted micromotors was highly desirable to improve the binding capacity, as well as enabled the equilibrium to be achieved within a shorter period of time. Fig. S3† indicates that a short time (20 min) offered convenient isolation of the target protein. Therefore, the concentration dependence of the magnetically imprinted micromotor for protein interaction was evaluated by using a time of 20 min.

The adsorption isotherm experiments for the micromotor sensor were carried out in various concentrations of phycocyanin solution for 20 min incubation, ranging from  $0\text{--}1 \text{ mg mL}^{-1}$ , and then thoroughly washed, and imaged with a fluorescent microscope. Fig. S4A–D display images of the magnetically imprinted micromotor sensor along with increasing initial concentrations. A gradual increase in the fluorescence intensity was observed as the phycocyanin concentration increased. As seen in Fig. S4,† the corresponding plot of fluorescence intensity *versus* concentration showed a nearly linear dependence up to  $0.75 \text{ mg mL}^{-1}$  phycocyanin. At equilibrium concentrations higher than  $1.0 \text{ mg mL}^{-1}$ , adsorption of the micromotor became stable and its recognition sites were almost saturated. The fluorescence intensity could thus provide a rough quantitative estimation of the protein concentration.

So, the resulting magnetically imprinted micromotor sensor offered direct recognition, capture, and transport, and the fluorescent target protein provided real-time optical visualization images of the MIP binding event based on changes in the fluorescence intensity. Furthermore, specific binding is a key

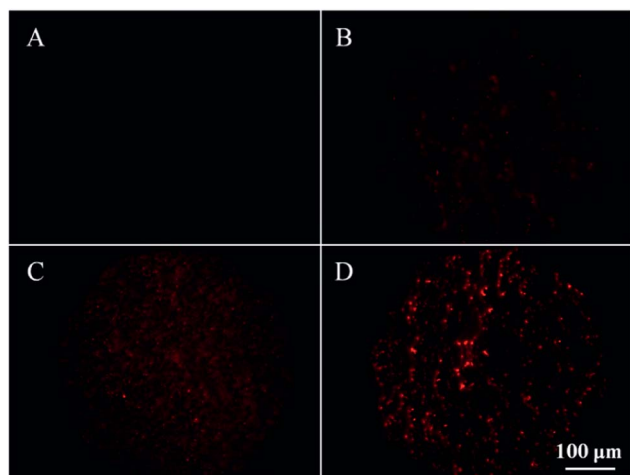


Fig. 5 Fluorescence microscope photos of the magnetically imprinted micromotor for 20 min in a solution containing increasing concentrations of phycocyanin target protein: (A) 0, (B) 0.5, (C) 0.75, and (D) 1 mg mL<sup>-1</sup>.

requirement for the new MIP-based microsensor isolation platform. Thus, control experiments were required to evaluate the binding specificity of the phycocyanin-imprinted microsensor toward phycocyanin, as seen in Fig. S5.† The NIP PEDOT/PSS microsensor did not emit apparent fluorescence (Fig. S5B†), suggesting that the microsensor could not bind the template protein, despite the fact that it was soaked in a higher concentration of phycocyanin solution for a long time. As well, the phycocyanin-imprinted microsensor showed no fluorescence after soaking for 20 min in a solution containing the protein BSA (Fig. S5C†). At the same time, through ultraviolet absorption spectra, the BSA concentration still showed no obvious change before and after being soaked in the solution. Therefore, the specificity of the MIP–PEDOT/PSS microsensor was clearly demonstrated, showing the crucial role of the MIP recognition sites in attaining such efficient and selective uptake of the target protein, and the negligible nonspecific adsorption onto the PEDOT/PSS outer polymer surface.

Moreover, due to the highly cross-linked polymeric and deposited metal nature, the MIP microsensor showed good physical stability and chemical inertness. Further analysis and regeneration of the microsensor could be accomplished by elution with a regeneration solution to take off the rebinding protein followed by rinsing with a neutral PBS to restore the neutral blank status. Such elution did not compromise the movement and combining ability of the microsensor. Furthermore, the microsensor was demonstrated to have excellent reproducibility due to the recoverability up to 5 cycles with the standard error within 10%. As for the long time stability, the MIP microsensor had been shown to be stable even after 90 days of their preparation when it was stored at 4 °C in a refrigerator.

### 3.5 Applications of the microsensor to seawater samples

In order to evaluate the practical utility of the developed MIP microsensor for phycocyanin recognition and transport,



Fig. 6 (A) Microscope photo of the magnetically imprinted micromotor in seawater with the target phycocyanin protein; (B) fluorescence time-lapse photo taken after the micromotor moved in seawater with phycocyanin for 20 min; (C) microscope photo of the micromotor after evaporation of the solution.

unprocessed natural seawater samples were used for further investigation. As shown in Fig. 6A, the efficient propulsion of the MIP microsensor in the seawater samples at speeds of  $78.8 \pm 2.9 \mu\text{m s}^{-1}$  allowed their prolonged movement and direct isolation of phycocyanin without tedious sample processing steps. The change in the speed (usually higher than  $100 \mu\text{m s}^{-1}$  above mentioned) could be ascribed to the viscosities and matrix effects of seawater, and the adsorption of molecules onto the catalytic Pt layer. Fig. 6B clearly illustrates the effective accumulation of the target phycocyanin onto the microsensor from phycocyanin-spiked seawater samples during the 20 min interaction. Such efficient binding was not compromised by the presence of a large excess of coexisting ions in the seawater samples. As seen in Fig. 6C, after evaporation, a large amount of seawater salt was left on the glass surface, and fortunately, it did not affect the phycocyanin adsorption in the microsensor. Overall, Fig. 6 supported the high specific enrichment ability of the MIP based microsensor, and confirmed its feasibility for isolation and transport of the target protein in complex samples.

In the complex seawater matrices, the target phycocyanin recognition should be coupled with effective discrimination against coexisting compounds and salts. Because the fluorescence intensity of the micromotor outside surface was weak, the fluorescence on the surface of the micromotor was required to be captured by time-lapse photos, and therefore the video of the moving fluorescence micromotor could not be directly taken. So, in order to get the video, the fluorescent phycocyanin protein was added to the solution to produce fluorescence, while the bubbles induced by the micromotor had no fluorescence, and thereby through a contrast, a real-time video could be taken. As recorded in ESI Video 4,† the phycocyanin adsorption did not interfere with the efficient bubble propulsion. The video results further indicated that the MIP micromotor sensor could realize real-time visualization imaging in complex samples, along with effective propulsion and recognition/capture of phycocyanin. Consequently, algae bloom monitoring and removal could be performed since phycocyanin is often used as the index of cyanobacteria.

## 4. Conclusions

In summary, a simple and rapid magnetically imprinted micromotor sensor with high selectivity and sensitivity was developed by combining MIPs and catalytic microtubules,

based on the porous PEDOT/PSS template assisted sequential electrodeposition protocol, and was successfully applied to effective label-free fluorescent phycocyanin recognition and transport. By taking full advantage of the custom-tailored MIPs, as well as the catalytic, magnetic and electrochemical responsive properties, the obtained microsensor easily realized the specific identification, autonomous adsorption/enrichment, and controllable motion of phycocyanin, even targeted directional transport and isolation from seawater matrices. The present phycocyanin imprinted microsensor opens promising prospects for the development of MIP-based platforms for the selective isolation and sensitive sensing of various target analytes coupled with the construction of self-propelled micro/nanoscale objects. Such studies will greatly contribute to marine pollution monitoring and abatement, extend the research connotations of concerned-target imprinting, as well as push forward the development of intelligent micro/nano-scale apparatus and strategies.

## Acknowledgements

This work was financially supported by the National Natural Science Foundation of China (21275158, 21477160), the Strategic Priority Research Program of the Chinese Academy of Sciences (XDA11020405), the Innovation Projects of the Chinese Academy of Sciences (KZCX2-EW-206), and the Scientific Research Foundation for the Returned Overseas Chinese Scholars, State Education Ministry.

## Notes and references

- 1 X. Chuai, W. Ding, X. Chen, X. Wang, A. Miao, B. Xi, L. He and L. Yang, *Ecol. Eng.*, 2011, **37**, 842–849.
- 2 M. Gantar, D. Simović, S. Djilas, W. W. Gonzalez and J. Mikšovska, *J. Biotechnol.*, 2012, **159**, 21–26.
- 3 J. N. Boyer, C. R. Kelble, P. B. Ortner and D. T. Rudnick, *Ecol. Indic.*, 2009, **9**, 1188–1197.
- 4 K. Song, L. Li, Z. Li, L. Tedesco, B. Hall and K. Shi, *Ecol. Informat.*, 2013, **15**, 22–33.
- 5 K. Song, L. Li, L. Tedesco, S. Li, B. Hall and J. Du, *ISPRS J. Photogramm. Remote Sens.*, 2014, **95**, 68–80.
- 6 N. T. Eriksen, *Appl. Microbiol. Biotechnol.*, 2008, **80**, 1–14.
- 7 Z. Zhang, L. Chen, F. Yang and J. Li, *RSC Adv.*, 2014, **4**, 31507–31514.
- 8 L. Chen, S. Xu and J. Li, *Chem. Soc. Rev.*, 2011, **40**, 2922–2942.
- 9 J. Li, Z. Zhang, S. Xu, L. Chen, N. Zhou, H. Xiong and H. Peng, *J. Mater. Chem.*, 2011, **21**, 19267–19274.
- 10 H. Liu, G. Fang and S. Wang, *Biosens. Bioelectron.*, 2014, **55**, 127–132.
- 11 M. J. Whitcombe, I. Chianella and L. Larcombe, *Chem. Soc. Rev.*, 2011, **40**, 1547–1571.
- 12 C. S. Mahon and D. A. Fulton, *Chem. Sci.*, 2013, **4**, 3661–3666.
- 13 S. Wang, J. Ye, Z. Bie and Z. Liu, *Chem. Sci.*, 2014, **5**, 1135–1140.
- 14 Z. Zhang, J. Li, J. Fu and L. Chen, *RSC Adv.*, 2014, **4**, 20677–20685.
- 15 D. Kagan, S. Campuzano, S. Balasubramanian, F. Kuralay, G. U. Flechsig and J. Wang, *Nano Lett.*, 2011, **11**, 2083–2087.
- 16 V. Garcia-Gradilla, J. Orozco, S. Sattayasamitsathit, F. Soto, F. Kuralay, A. Pourazary, A. Katzenberg, W. Gao, Y. Shen and J. Wang, *ACS Nano*, 2013, **7**, 9232–9240.
- 17 J. Wang and W. Gao, *ACS Nano*, 2012, **6**, 5745–5751.
- 18 G. Huang, J. Wang and Y. Mei, *J. Mater. Chem.*, 2012, **22**, 6519–6525.
- 19 J. Orozco, A. Cortés, G. Cheng, S. Sattayasamitsathit, W. Gao, X. Feng, Y. Shen and J. Wang, *J. Am. Chem. Soc.*, 2013, **135**, 5336–5339.
- 20 M. J. Banholzer, L. Qin, J. E. Millstone, K. D. Osberg and C. A. Mirkin, *Nat. Protoc.*, 2009, **4**, 838–848.
- 21 J. Li, G. Huang, M. Ye, M. Li, R. Liu and Y. Mei, *Nanoscale*, 2011, **3**, 5083–5089.
- 22 W. Gao, S. Sattayasamitsathit, A. Uygun, A. Pei, A. Ponedal and J. Wang, *Nanoscale*, 2012, **4**, 2447–2453.
- 23 W. Gao, A. Pei, X. Feng, C. Hennessy and J. Wang, *J. Am. Chem. Soc.*, 2013, **135**, 998–1001.
- 24 M. Manjare, B. Yang and Y. Zhao, *J. Phys. Chem. C*, 2013, **117**, 4657–4665.
- 25 D. Yamamoto, A. Mukai, N. Okita, K. Yoshikawa and A. Shioi, *J. Chem. Phys.*, 2013, **139**, 034705.
- 26 M. García, J. Orozco, M. Guix, W. Gao, S. Sattayasamitsathit, A. Escarpa, A. Merkoçi and J. Wang, *Nanoscale*, 2013, **5**, 1325–1331.